



Efficient degradation of clofibric acid by electro-enhanced peroxydisulfate activation with Fe-Cu/SBA-15 catalyst

Heng Lin^a, Xin Zhong^{a,1}, Carmen Ciotonea^b, Xiaohui Fan^a, Xiaoyu Mao^a, Yating Li^a, Bin Deng^a, Hui Zhang^{a,*}, Sébastien Royer^{b,*}

^a Department of Science and Environmental Engineering, Hubei Environmental Remediation Material Engineering Technology Research Center, Wuhan University, P.O. Box C319, Luoyu Road, 129#, Wuhan 430079, PR China

^b Univ. Lille, CNRS, ENSCL, Centrale Lille, Univ. Artois, UMR 8181 – UCCS – Unité de Catalyse et de Chimie du Solide, F-59000 Lille, France



ARTICLE INFO

Keywords:

Clofibric acid
Sulfate radical
Hydroxyl radical
Heterogeneous catalysis
Electrochemical reaction

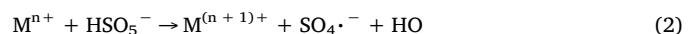
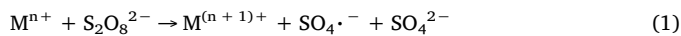
ABSTRACT

Mesoporous silica supported mono and bimetallic oxides are employed for the degradation of clofibric acid (CFA) in the heterogeneous electro-enhanced persulfate activation system. The oxidation system includes heterogeneous peroxydisulfate (PDS, $S_2O_8^{2-}$) activation coupled with electrochemical process, leading to the production of highly reactive radicals ($SO_4^{\cdot -}$ and $\cdot OH$). The influence of degradation reaction parameters, amongst the initial solution pH, current density, $S_2O_8^{2-}$ concentration and catalyst loading, is investigated. Efficiency of catalyst to generate reactive radicals is confirmed using electron paramagnetic resonance (EPR) analysis and radical quenching experiments. The catalytic performance was evaluated in terms of CFA concentration abatement, while the stability of catalyst is followed by quantifying the metal leaching into the aqueous solution during reaction and the evolution of surface characteristics of the materials before and after reaction. The main degradation intermediates were identified in order to propose a possible degradation pathway of CFA.

1. Introduction

Residual molecules from pharmaceutical drugs and their metabolic products found in the environment have attracted continuous recent interest. Although they are prevalent at low concentrations, these compounds are often detected and considered as emerging environmental contaminants, due to their potential influences on the development of living organisms and of the ecosystem, and obviously on human health [1,2]. As one of these emerging pollutants, clofibric acid (CFA), which is the metabolite of clofibrate drugs (a blood lipid regulator), shows long-term durability in the aquatic environment and is hardly removed using conventional water purification processes [3–6].

Recently, sulfate radical ($SO_4^{\cdot -}$, SR) based advanced oxidation processes (AOPs) have attracted great concern [7–9]. Compared with hydroxyl radical, sulfate radical demonstrates a similar oxidation potential, associated with longer half-life under neutral pH condition [10,11]. Generally, peroxymonosulfate (PMS, HSO_5^-) or peroxydisulfate (PDS, $S_2O_8^{2-}$) is activated over transition metal (M^{n+}) to produce sulfate radicals [12,13]:



Nevertheless, several drawbacks issued from the homogeneous activation approach limit the development of M^{n+} activating persulfate (PS) processes. For example, the regeneration of lower-charged ion is difficult after its conversion to higher-charged ion, so large amounts of metal ions are needed to activate persulfate [14]. In addition, the generated metal sludge displays adverse effects on the environment and needs further treatment and disposal [15].

Inspired by the Fered-Fenton process, in which H_2O_2 and Fe^{2+}/Fe^{3+} were added into an electrolytic cell [16–18], the above drawbacks could be overcome with the combination of iron activating PS process and electrochemical oxidation process, namely electro/Fe(II,III)/PS process. The activation of PS by Eq. (1) or (2) is then enhanced by the continuous electro-regeneration of Fe^{2+} species via cathodic reduction during electro/Fe(II,III)/PS process (Eq. (3)) [8]. Meanwhile, in electrochemical oxidation process, target contaminants can also be degraded by hydroxyl radicals generated on the surface of high oxygen overvoltage anodes (Eq. 4), such as dimensionally stable anode (DSA), Pt and boron-doped diamond (BDD) anode [19].

* Corresponding authors.

E-mail addresses: eeng@whu.edu.cn (H. Zhang), sebastien.royer@univ-lille1.fr (S. Royer).

¹ Co-first author.



So far, the homogeneous electro-enhanced iron activating PS process has been applied to treat landfill leachate [20] and refractory pollutants such as Orange II [21], bisphenol A [22] and CFA [6].

Compared with homogeneous activation, the heterogeneous activation of PS has developed quickly because the solid catalysts are easily separated from the effluent for reuse [23]. Moreover, the heterogeneous system is effective over a broader pH range including the common pH for natural water and wastewater (pH 2–9) [23]. Therefore, iron-based catalysts, such as Fe_2O_3 , Fe_3O_4 and Fe° , are commonly employed as catalysts to activate persulfate [23]. Recent researches imply the combination of copper with iron to fabricate iron–copper bimetallic nanoparticles exhibiting an improved catalytic activity due to the interaction between the two-metal redox couples [24,25]. Nevertheless, nanoparticles always trend to aggregate under reaction, because of their inherent high surface energy, which leads to detrimental catalytic properties [25]. Therefore, the use of porous materials, such as allophane [26], mesoporous carbon [27] and mesoporous silica materials [28,29], has been proposed. Among them, mesoporous SBA-15 silica exhibits sufficient stability in aqueous solution at low temperature, rendering it very attractive for liquid phase reaction [28]. Therefore, mesoporous silica can be a promising support for the immobilization of iron–copper bimetallic nanoparticles and have been used in heterogeneous activation processes [28–30]. Generally, the high valence metals in bimetallic catalysts are less reactive towards persulfate activation [31], unless they can be reduced to low valence ones. The introduction of electrochemical process can favor the reduction of high valence metals to low valence metals, and promote the continuous regeneration of low valence metals on catalyst surface to retain high persulfate activating efficiency [31,32].

In this study, Fe–Cu containing catalyst was proposed as a friendly catalytic composition, and its properties for the electrochemical/heterogeneously activated PDS process were studied for the degradation of CFA. Catalytic performances were evaluated by the measurement of CFA concentration. Degradation mechanisms of CFA oxidation were investigated by detecting the reactive radicals generated in the electro/catalyst/ $\text{S}_2\text{O}_8^{2-}$ process and evaluating the modifications of the catalyst surface after oxidation reaction. Furthermore, the intermediate reaction products were identified to propose a plausible degradation reaction pathway of CFA degradation.

2. Materials and methods

2.1. Materials

The materials and methods used in this study are listed in the Supplementary Material (Text S1).

2.2. Preparation and characterization of heterogeneous catalyst

SBA-15 silica is synthesized according to previously established protocol [33]. 4 g of Pluronic P123 ($\text{PEO}_{20}\text{-PPO}_{70}\text{-PEO}_{20}$) is dissolved in 150 mL of HCl solution (1.6 M) at 40 °C. Then 8.5 g of tetraethyl orthosilicate (TEOS) is added dropwise to the solution, and magnetic stirring is maintained for 24 h. The resulting gel is submitted to hydrothermal treatment for 48 h at 100 °C. After recovering by filtration, washing with water, and drying, the material is calcined at 550 °C for 6 h (muffle furnace, heating ramp of 1.5 °C min⁻¹).

Transition metal oxide containing catalysts were prepared using the *in situ* auto-combustion approach [34,35]. The total metal loading is fixed at 5 wt.% (Cu + Fe, metal basis). In a first step, nitrate precursors are dissolved in water (10 mL), and glycine is added dropwise to the solution (glycine to NO_3^- molar ratio of 1). Thereafter, the support is

gently mixed with the solution containing the metal precursors and glycine, and the mixture is aged for 3 h. The evaporation of the solvent is performed at 100 °C, and the dry powder is subjected to the glycine combustion step (300 °C). The catalysts are finally calcined at 500 °C for 6 h (1.5 °C min⁻¹). The samples were named tM₁·tM₂/SBA (where t = the metal loading in wt.%, M₁ = Fe and M₂ = Cu). The characterization techniques for catalysts were presented in the Supplementary Material (Text S2).

2.3. Electrolytic apparatus and procedures

The experiments were performed in a 250 mL glass beaker containing 200 mL of solution. The reactor was immersed in a water bath to keep the temperature constant at 20 ± 2 °C. A Model WYK-305 direct current (DC) power supply from Yangzhou Jintong Source, Co., Ltd. (China) was employed to provide the constant current. One pair of 5 cm × 11.9 cm plate anode ($\text{Ti}/\text{RuO}_2\text{-IrO}_2$) and plate cathode (titanium plate) from Baoji Xinyu Optics-Mechanics-Electricity Co. LTD (China) was positioned in the middle of the reactor, at a distance of 3.0 cm to each other in the reactor. In a typical run, 0.1 mM CFA was freshly prepared in buffer solution. Solutions at different pH were obtained as follow: 0.05 mol L⁻¹ H_3PO_4 – 0.1 mol L⁻¹ of NaOH solution to obtain a pH of 9.0; 0.05 mol L⁻¹ Na_2HPO_4 and NaH_2PO_4 to obtain pH values of 5.0 and 6.5; 0.05 mol L⁻¹ H_3PO_4 – 0.05 mol L⁻¹ NaH_2PO_4 to obtain pH of 3.0 [36]. At the beginning of an experiment, known amounts of $\text{S}_2\text{O}_8^{2-}$ and catalyst were added into the CFA solution under magnetic stirring. Reaction solution was sampled at fixed time intervals for analysis.

2.4. Analysis of reaction solutions and used catalysts

CFA concentration is quantified by using a high performance liquid chromatography (HPLC, Shimadzu) equipped with a LC-20AB pump, a Shimadzu HPLC System Manager program and a SPD-10A UV-Vis detector at maximum absorption wavelength of 230 nm which was determined by a Shimadzu UV-1600 spectrophotometer in the wavelength range of 200–800 nm. An acetonitrile/0.01 M aqueous oxalic acid (31:69, v/v) mixture is used as mobile phase with a constant flow rate of 1.0 mol L⁻¹. Reaction products are analyzed by liquid chromatograph - mass spectrometer (LC-MS, Agilent 1290-LC/6460-MS) with electrospray ionisation operating in positive and negative mode. The mass spectrometer scans in the 100–500 m/z range.

The concentration of PDS was analyzed using an iodometric titration method (Text S3) [37]. Metal leaching (Cu, Fe) is systematically evaluated by atomic absorption spectroscopy (AAS, Perkin Elmer AA-nalyst 800), quantifying the solubilized metal concentrations.

Electron paramagnetic resonance (EPR) signals of reactive radicals trapped by DMPO (a typical spin-trap agent for $\cdot\text{OH}$ and $\text{SO}_4^{\cdot-}$) were detected on a JES-FA200 spectrometer at room temperature with center field of 3260 G, sweep width of 100 G, microwave frequency of 9.14 GHz, microwave power of 3 mW, modulation frequency of 100 KHz, modulation amplitude of 10 G time constant of 0.03 s and sweep time of 30 s.

3. Results and discussion

3.1. Characterization of catalysts

3.1.1. Structural properties of supported metal oxide phases

The small angle X-ray Diffraction (XRD) diffractograms of SBA-15 and of derived catalysts are presented in Fig. 1(a). All patterns are presenting three well-resolved peaks that are ascribed to the (100), (110) and (200) planes of p6mm hexagonal symmetry structures indicating an excellent pore structure uniformity. After the transition metal oxide (TMO) deposition, the first peak is slightly shifted to higher values and its intensity is slightly decreased. The hexagonal unit cell

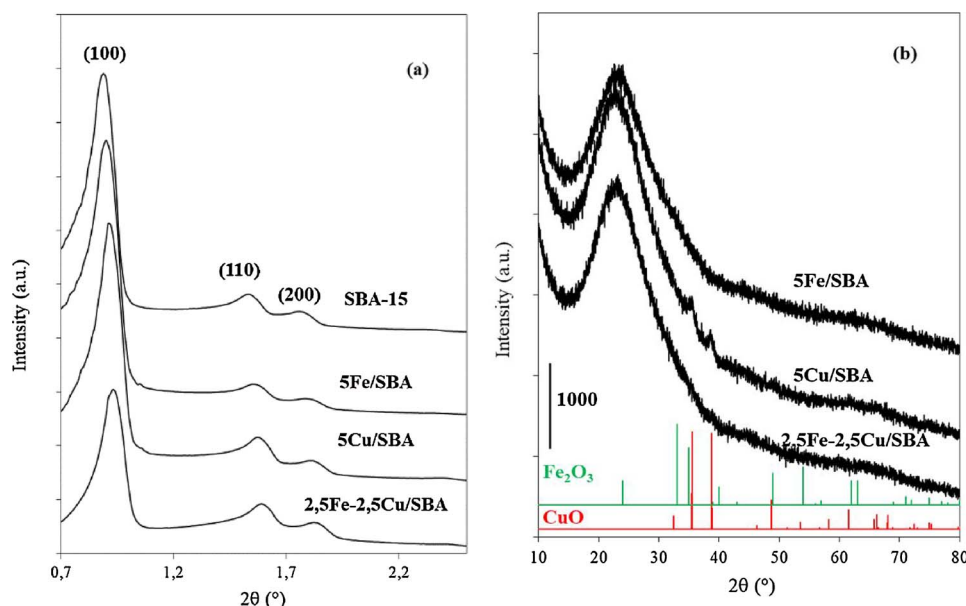


Fig. 1. Small angle (a) and wide angle (b) XRD patterns of SBA-15 and transition metal containing materials. Bottom: CuO reference (red) and Fe_2O_3 reference (green). (For interpretation of the references to colour in this figure legend, the reader is referred to the web version of this article.)

Table 1
Textural properties of SBA-15 and transition metal containing catalysts.

| Sample | a_0 (nm) ^a | S_{BET} ^b ($\text{m}^2 \text{g}^{-1}$) | V_{pore} ^c ($\text{cm}^3 \text{g}^{-1}$) | D_p ^d (nm) |
|-----------------|-------------------------|--|--|-------------------------|
| SBA-15 | 11.3 | 819 | 1.20 | 7; 7.7 |
| 5Fe/SBA | 11.2 | 565 | 0.89 | 6.7; 7.6 |
| 2,5Fe-2,5Cu/SBA | 11.1 | 563 | 0.80 | 6.7; 7.5 |
| 5Cu/SBA | 10.9 | 471 | 0.89 | 7; 7.7 |

^a unit-cell parameter.

^b specific surface area.

^c total pore volume.

^d pore size.

parameter was calculated from (100) reflection position (Table 1). No significant modification of the unit cell parameter, from 11.3 nm (SBA-15) to 10.9 nm (5Cu-SBA), is measured. These low angle XRD results indicate that TMO formation process does not affect long range ordering of pore network of the SBA-15 when prepared by *in situ* auto-combustion approach, as previously observed [35,38].

The high angle XRD patterns recorded for the different materials are presented in Fig. 1(b). For 5Fe/SBA and 2,5Fe-2,5Cu/SBA, no reflections characteristic of iron oxide phase or copper oxide phase can be detected. Then, oxide (copper oxide, or iron oxide) forms on the surface of silica as small nano-particles (NPs), as previously observed for the synthesis of various supported metal oxides using this approach [34,35,38]. The limited size of the formed particles, meaning the high dispersion of the transition metal phase, avoids the detection of well-defined reflections by XRD. In the case of 5Cu/SBA, two poorly defined reflections are observed at $20 \sim 36^\circ$ and 39° . These two reflections are characteristic of the CuO phase (PDF file No. 048-1548).

3.1.2. Textural properties of materials

The N_2 adsorption/desorption isotherms obtained for the different materials are presented in Fig. 2(a). Calculated textural properties are gathered in Table 1. The isotherms are all of type IV with a hysteresis loop type of H1. Isotherm shape is characteristic of mesoporous materials, while H1-type hysteresis confirms the maintaining of well-ordered, regular, cylindrical pores. Then, N_2 physisorption results confirm that the ordered pore structure of the host support is mostly not altered by the *in situ* auto-combustion deposition, as already obtained in previous studies [38] and confirmed by low angle XRD analysis (Fig. 1(a)).

Deposition of the TMO NPs in the SBA-15 pores induces a decrease of the material surface area, which is observed to decrease by 30–40% (Table 1). In addition, pore volume is observed to decrease in a similar proportion. Pore size distribution (Fig. 2(b)) shows no significant modification. The evolution of the pore volume is coherent with a mesopore fraction filling by the impregnated phase, while the few modification of the pore size distribution is coherent with the formation of small size NPs in the support tubular porosity.

3.1.3. Reducibility of supported metal oxide nanoparticles

Reducibility of transition metal oxide NPs in catalysts is evaluated by Hydrogen Temperature-Programmed Reduction (H_2 -TPR). Thermograms are presented in Fig. 3, and main temperatures of reduction and reduction degrees are gathered in Table 2. Reduction of 5Fe/SBA is observed to proceed in two successive steps. A first hydrogen consumption peak, with the maximum of consumption located at 405°C , is observed. Thereafter, a second more intense hydrogen consumption peak, with a maximum hydrogen consumption located at 1015°C , is also observed. This two-step reduction process is coherent with the reduction of Fe_2O_3 phase, with: (i) at low temperature, the reduction of Fe^{3+} into Fe^{2+} (with formation of FeO intermediate phase); and (ii) at high temperature, the reduction of Fe^{2+} to Fe^0 [39,40]. Amount of hydrogen experimentally consumed fits well with the theoretical amount to be consumed for the complete reduction of Fe_2O_3 into Fe^0 (Table 2, with reduction degree $> 90\%$), confirming the previous interpretation.

Reduction of 5Cu/SBA is observed to occur in one step, with only one hydrogen consumption peak observed centered at $T = 238^\circ\text{C}$. This hydrogen consumption is ascribed to the reduction of CuO phase into metallic Cu. Amount of hydrogen experimentally consumed is also fitting with the theoretical amount to completely reduce Cu^{2+} species into Cu^0 (Table 2, reduction degree close to 90%). Due to the single reduction and its position in terms of temperature, this consumption can be ascribed to the reduction of small CuO particles [41].

The reduction of 2,5Cu-2,5Fe/SBA is observed to proceed in two steps: (i) a first hydrogen consumption peak observed at $234\text{--}255^\circ\text{C}$, followed by (ii) a second one at 948°C . Then, the first hydrogen consumption peak is ascribed to the reduction of CuO into metallic Cu^0 . The amount of hydrogen consumed experimentally however exceeds the theoretical one, meaning that the reduction of Fe^{3+} species into Fe^{2+} species occurs in the same temperature range. The reduction of

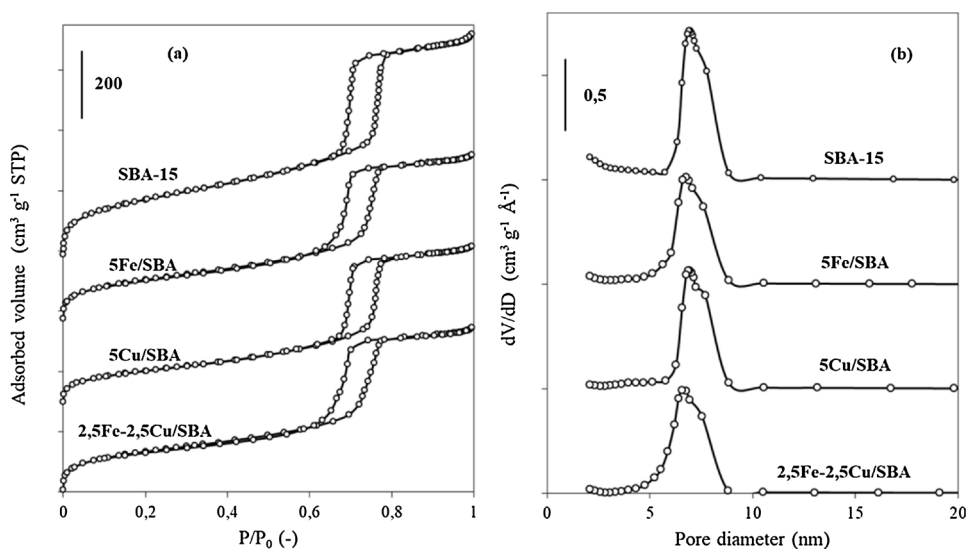


Fig. 2. N₂ adsorption-desorption isotherms (a) and B.J.H. pore size distribution (b) of SBA-15 and transition metal containing materials.

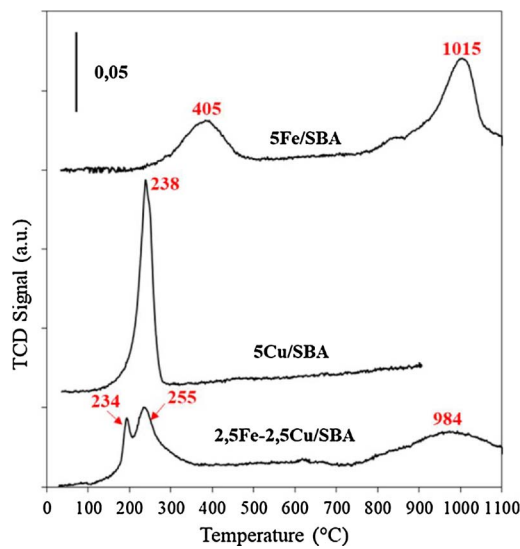


Fig. 3. H₂-TPR profiles recorded over transition metal containing materials.

Table 2
Results of H₂-TPR of transition metal containing catalysts.

| Sample | Reduction temperature | | Experimental amount of H ₂ consumed (mmol g ⁻¹) | Theoretical amount of H ₂ to reduce to metal (mmol g ⁻¹) | Fe ³⁺ / Cu ²⁺ reduction degree to metal (%) |
|-----------------|-----------------------|----------------------|--|---|---|
| | T _{LR} (°C) | T _{HR} (°C) | | | |
| 5Fe/SBA | 405 | 1015 | 1.29 | 1.34 | 96 |
| 2,5Fe-2,5Cu/SBA | 255 | 984 | 1.03 | 1.06 | 97 |
| 5Cu/SBA | 238 | – | 0.69 | 0.79 | 87 |

T_{LR}, low reduction temperature; T_{HR}, high reduction temperature; Transition metal reduction degree is calculated using the exact TM content in the materials as evaluated by ICP-OES, and assuming CuO and Fe₂O₃ as initial phases.

the Cu-Fe containing material is not a linear combination of the reduction of the Cu- and of the Fe-containing materials, and the reduction of Fe³⁺ species is observed to be shifted to the lower temperatures in the presence of copper (shifting from 405 °C in 5Fe/SBA, to 255 °C in 2,5Fe-2,5Cu/SBA). Finally, the high temperature hydrogen consumption peak, being located at 984 °C is ascribed to the reduction of Fe²⁺

into Fe⁰, due to the close proximity in terms of temperature with the high temperature reduction peak for the 5Fe/SBA material, and a global reduction degree of ionic species into metal close to 100% (Table 2). The presence of copper phase then facilitates the reduction of the iron phase. Such phenomenon was already observed in the literature and was ascribed to modification of iron and copper phases dispersion modification as well as changes in activation energy of the iron phase reduction process [42,43].

3.1.4. Active phase morphology

Transmission Electron Microscopy (TEM) images, obtained for the three catalysts, are presented in Fig. 4. First, the hexagonal arrangement of the silica support is clearly observed throughout all materials, confirming the limited impact of the preparation route on the support porosity quality.

For 5Fe/SBA catalyst, the detection of iron particle is difficult (Fig. 4(a)). Then, compared with material prepared by classical impregnation (wet impregnation, incipient wetness impregnation), iron oxide does not form particles confined in main mesopores [33]. However, Energy Dispersive X-ray Spectroscopy (EDXS) analysis confirms the presence of Fe inside the silica grains, with average values (20 analyses) of Fe weight content of 5.43% in silica grain despite formation of visible bulky particles at low magnification. Increasing magnification of observation allows to detect very small pseudo-spherical particles, of size always below 2 nm, located throughout the silica grains, in addition to few filamentous iron oxide particles located on the periphery of the silica grains (thickness of less than 3 nm). These observations are in accordance with XRD results for which no clear reflections (characteristic of bulk oxide phase) can be observed (Fig. 1).

For 5Cu/SBA, copper phase is also difficult to observe inside the silica grains. As in the case of 5Fe/SBA, EDXS analysis confirms the presence of copper located inside all the analyzed silica grains (Fig. 4(b)), 5Cu/SBA(2) and associated EDX spectra), in addition to visible formation of mesopore confined ~10 nm CuO NPs in very few areas (example given in Fig. 4(b), 5Cu/SBA(1) and (3)). This result is remarkable knowing the difficulties to efficiently disperse copper oxide over silica surface [44]. Indeed, using classical impregnation, most of the copper particles form as large particles located outside the silica porosity, or at least form as mesopore confined NPs. Then, the approach used here ensures the maintaining of high copper oxide dispersion. These results are coherent with XRD results for which poorly defined reflections ascribed to CuO phase are detected in the baseline noise of the diffraction signal, which probably originates from the mesopore confined NPs.

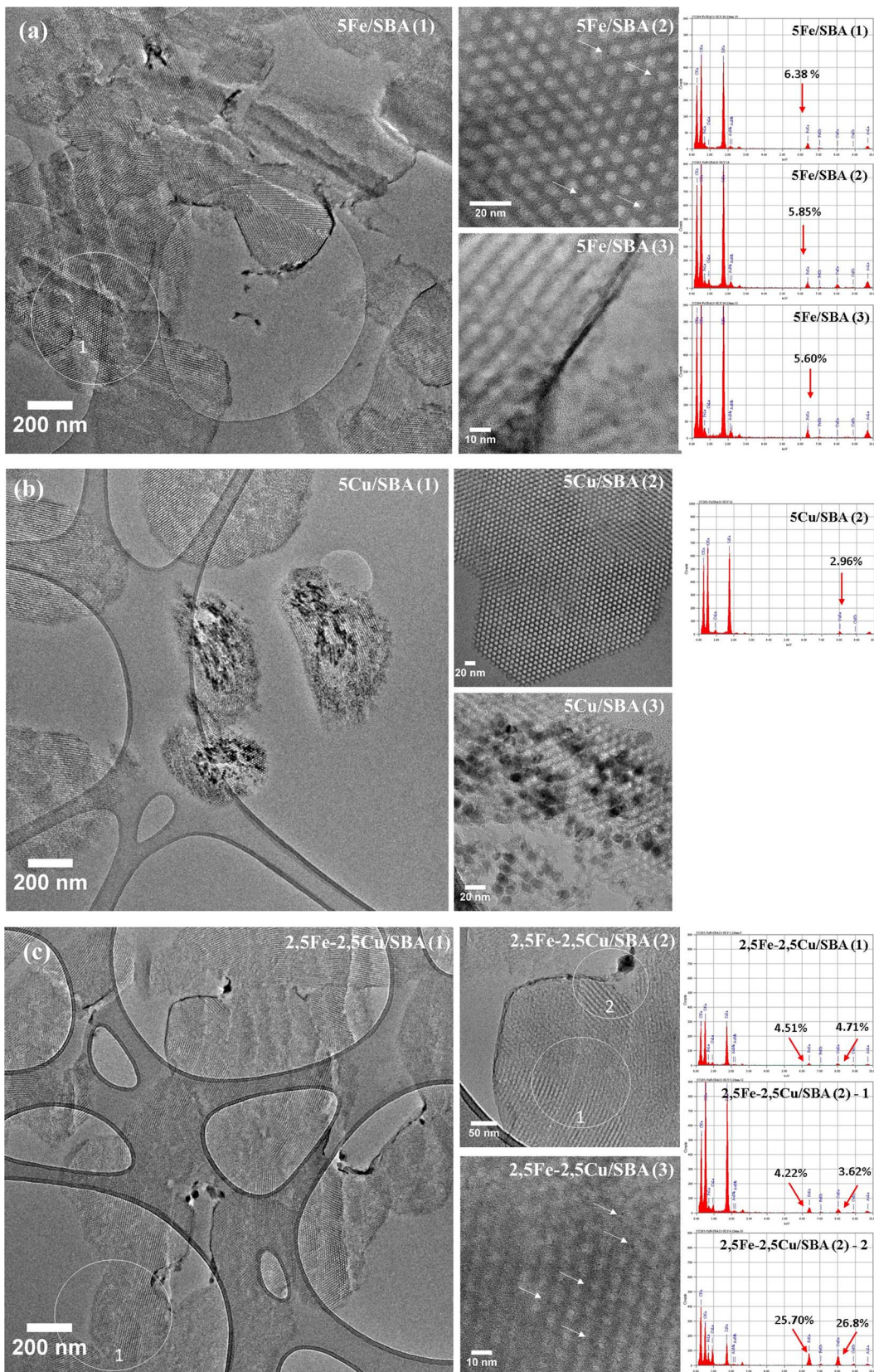


Fig. 4. Representative TEM images and punctual EDXS analyses recorded for 5Fe/SBA, 5Cu/SBA and 2,5Fe-2,5Cu/SBA catalysts.

Finally, for 2,5Fe-2,5Cu/SBA, comparable results are obtained with most of the CuO and Fe₂O₃ observed inside the silica porosity (confirmed by EDXS analysis), in the form of particles, of size largely below the mesopore sizes (Fig. 4(c), 2,5Fe-2,5Cu/SBA(3)). Very few external

particles of limited size can be observed on the periphery of the silica grains (see low magnification image). EDXS analysis also gives confirmation of the presence of Cu and Fe in all analyzed zones (Fe/Cu weight ratios being always ranging at 1.0 ± 0.2 , see the three EDX

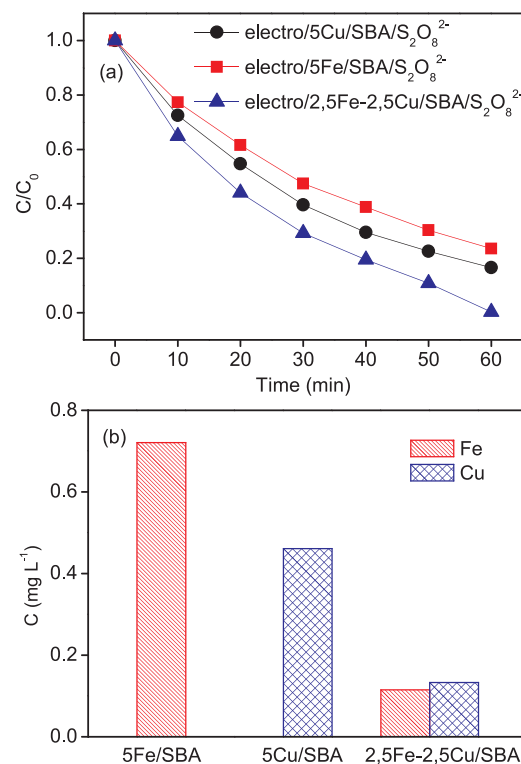


Fig. 5. (a) Clofibric acid degradation with reaction time; (b) metal ion leaching quantified on the liquid phase, after 60 min of reaction. Reaction conditions: $j = 16.8 \text{ mA cm}^{-2}$, $[\text{S}_2\text{O}_8^{2-}] = 10 \text{ mM}$, catalyst loading = 0.5 g L^{-1} , pH 6.5.

spectra presented).

3.2. Efficiency of bimetallic vs. monometallic nanoparticles for CFA degradation

Activity of the different catalysts for the degradation of CFA, is presented in Fig. 5(a). Degradation efficiency of 83.4% after 60 min of reaction is obtained for 5Cu/SBA. Lower degradation efficiency is observed for 5Fe-SBA, with only 76.4% of CFA concentration abatement obtained after 1 h of reaction. Significantly higher degradation efficiency is obtained for the 2,5Cu-2,5Fe/SBA for which 99.7% of the initial CFA concentration abatement is obtained after 60 min of reaction. This result clearly shows the benefit of using bimetallic material instead of monometallic material to reach high CFA degradation degree, as already reported for other pollutants [29]. More efficient catalytic activity, reached during reaction over Cu-containing materials, can be related to the improvement in reducibility, as observed in Fig. 3 and Table 2.

The remaining fraction of PDS, at the end of the reaction, is 48.4%, 32.3% and 26.6%, for 5Fe-SBA, 5Cu-SBA and 2,5Fe-2,5Cu/SBA respectively (Figure S1). The PDS consumption is consequently directly following CFA degradation degree.

Metal ions leaching during reaction was evaluated at the end of the reaction cycle (Fig. 5(b)). Concentrations of metal ion in solution at the end of the reaction are: 0.72 mg L^{-1} of Fe for 5Fe-SBA, and 0.46 mg L^{-1} of Cu for 5Cu-SBA. Significant decrease in metal ion leaching is observed over the bimetallic materials, with only 0.12 mg L^{-1} of Fe and 0.13 mg L^{-1} of Cu leached in the solution at the end of reaction. Therefore, 2,5Fe-2,5Cu-SBA, besides more active, is also displaying significantly better stability toward leaching. This material is consequently used in the following oxidation experiments.

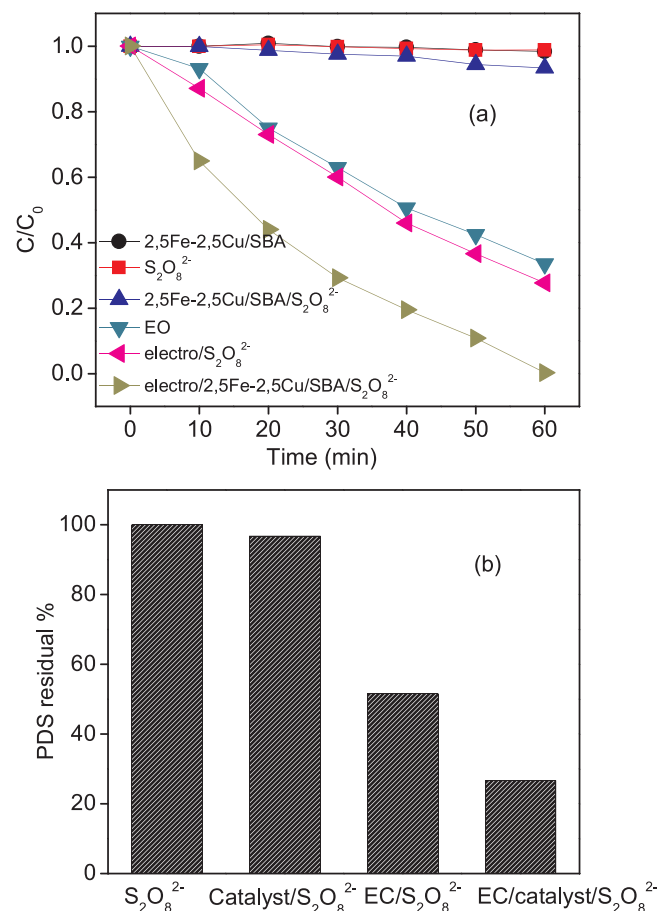


Fig. 6. (a) Degradation of clofibric acid under different reaction conditions, and (b) residual $\text{S}_2\text{O}_8^{2-}$ after 60 min of reaction. Reaction conditions: 2,5Fe-2,5Cu/SBA alone (catalyst loading = 0.5 g L^{-1}); $\text{S}_2\text{O}_8^{2-}$ alone ($[\text{S}_2\text{O}_8^{2-}] = 10 \text{ mM}$); 2,5Fe-2,5Cu/SBA + $\text{S}_2\text{O}_8^{2-}$ (catalyst loading = 0.5 g L^{-1} , $[\text{S}_2\text{O}_8^{2-}] = 10 \text{ mM}$); EO alone ($j = 16.8 \text{ mA cm}^{-2}$); electro/ $\text{S}_2\text{O}_8^{2-}$ ($j = 16.8 \text{ mA cm}^{-2}$, $[\text{S}_2\text{O}_8^{2-}] = 10 \text{ mM}$, catalyst loading = 0.5 g L^{-1}); all experiments are performed at 20°C and pH = 6.5.

3.3. Catalytic properties of 2,5Fe-2,5Cu-SBA

CFA degradation efficiency is evaluated under different reaction configurations (Fig. 6). Negligible CFA abatement occurs using the catalyst alone (no $\text{S}_2\text{O}_8^{2-}$, no electrochemical activation). This experiment demonstrated the poor affinity of the CFA with the catalyst surface, since no significant adsorption of CFA occurs (< 3% of CFA abatement). Using only $\text{S}_2\text{O}_8^{2-}$ (no catalyst, no electrochemical activation), no significant CFA degradation occurs, indicating that PDS decomposition into active radical does not proceed homogeneously. Under the reaction conditions regrouping in solution catalyst and $\text{S}_2\text{O}_8^{2-}$ (no electrochemical activation), CFA abatement remains very limited, staying < 10% after 60 min of reaction. The low efficiency under these conditions is originating from the limited ability to regenerate low charged ions from high charged ions reduction.

Using electrolysis alone (EO, no $\text{S}_2\text{O}_8^{2-}$, no catalyst), significant CFA degradation occurs. CFA removal then reaches 66.2% at the end of the 60 min of reaction. System efficiency is related to the production of hydroxyl radicals generated by water discharge at the DSA anode that provides active species for CFA degradation [45]. Only a slight increase in process efficiency is observed using the electro/ $\text{S}_2\text{O}_8^{2-}$ process, with CFA degradation reaching 72.3% after 60 min of reaction. This improvement is ascribed to the production of sulfate radicals by PDS activation in the electrochemical process [21], as depicted in Eq. (5). Under these conditions, 48.8% of PDS was decomposed after the

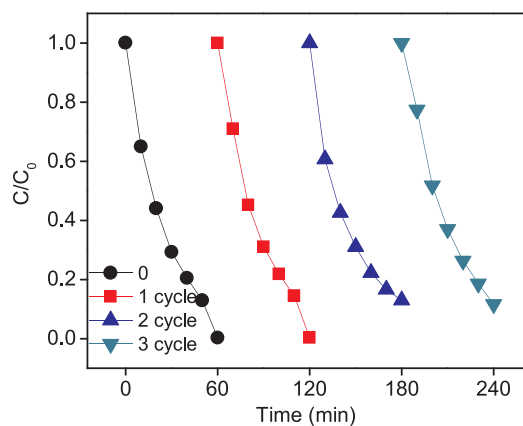


Fig. 7. Reusability of 2,5Fe-2,5Cu/SBA-15 catalyst. Reaction conditions: catalyst loading = 0.5 g L⁻¹; [S₂O₈²⁻] = 10 mM; pH = 6.5; j = 16.8 mA cm⁻².

reaction (Fig. 6(b)).



The electrochemical enhanced 2,5Fe-2,5Cu/SBA/S₂O₈²⁻ process (electro/2,5Fe-2,5Cu/SBA/S₂O₈²⁻ process) ensures almost complete CFA degradation in 60 min of reaction. Under these conditions, the lowest PDS residual is obtained (26%, Fig. 6(b)), indicating more important reactive radicals formation. Electrochemically assisted heterogeneous catalytic process is consequently the configuration ensuring the best efficiency for CFA abatement.

Optimization of reaction conditions was performed. Effect of catalyst concentration, initial pH, current density and PDS concentration are presented and discussed in the Supplementary Material (Text S4, including Figure S2).

3.4. Stability of the 2,5Fe-2,5Cu/SBA catalyst

The stability of the catalyst activity during the process is a major issue for such application. Recycling experiments are realized and results are presented in Fig. 7. It is observed that the CFA degradation efficiency slightly decreased with cycle number. Abatement, initially of 99.7%, is going to stabilize at a clofibric acid abatement of 88 ± 0.6% for the two last cycles. The slight decrease in abatement value can be related to the small leaching occurring for iron and copper, as observed during the first reaction cycle in Fig. 5(b). The above results show that the 2,5Fe-2,5Cu/SBA is durable and can be reused in reaction with limited loss of efficiency.

3.5. Mechanism of CFA degradation

3.5.1. Radical formation

Quenching experiments were performed to identify the formation of reactive radicals. Methanol (MeOH) is commonly used as scavenger to suppress the contributions of both ·OH and SO₄^{·-} radicals because it reacts with ·OH ($9.7 \times 10^8 \text{ M}^{-1} \text{s}^{-1}$) and SO₄^{·-} ($3.2 \times 10^6 \text{ M}^{-1} \text{s}^{-1}$) at similar rate constants [23]. Tert-butyl alcohol (TBA) is usually used as a selective ·OH scavenger to discriminate the contributions of ·OH and SO₄^{·-} (TBA reacts 1000-fold faster with ·OH ($3.8 - 7.6 \times 10^8 \text{ M}^{-1} \text{s}^{-1}$) than with SO₄^{·-} ($4 - 9.1 \times 10^5 \text{ M}^{-1} \text{s}^{-1}$) [46]). MeOH and TBA are hydrophilic compounds and are not suggested to accumulate near to/on the catalyst surface [47]. Therefore, MeOH and TBA are likely to scavenge free radicals in the solution [48]. Phenol, as a hydrophobic radical scavenger, can move close to the surface of catalyst due to the interaction between the delocalized p electrons of the oxygen-free Lewis basic sites and the free electrons of the target molecule present in the aromatic rings [49]. Moreover, phenol reacts with both ·OH ($6.6 \times 10^9 \text{ M}^{-1} \text{s}^{-1}$) and SO₄^{·-}

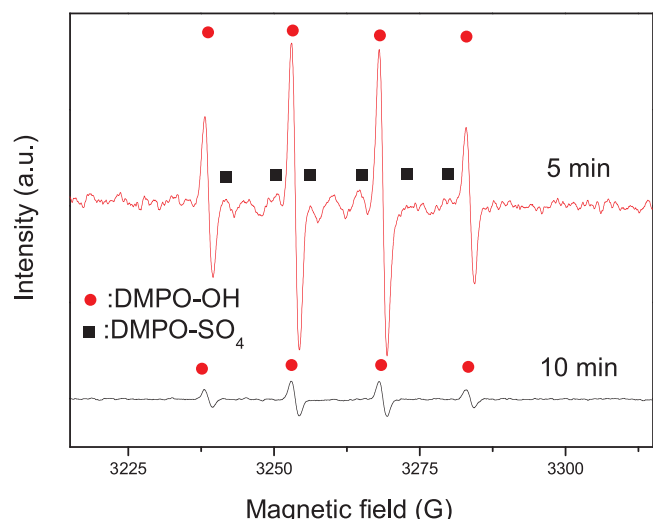


Fig. 8. EPR spectrum recorded at different reaction times. Reaction conditions: catalyst loading = 0.5 g L⁻¹; [S₂O₈²⁻] = 10 mM; j = 16.8 mA cm⁻²; pH = 6.5.

($8.8 \times 10^9 \text{ M}^{-1} \text{s}^{-1}$) at high rates and is suitable for scavenging of both radicals [50].

Evolution of clofibric acid abatement with reaction time in the presence of the different scavenging molecules is presented in Figure S3. CFA removal efficiency declined slightly from 97.2% to 80.6%, when 10 mM of TBA was added. It is confirming the presence of hydroxyl radicals in the solution. When 10 mM MeOH was used as scavenger, the CFA abatement curve (given a CFA abatement of 77.6% at 60 min of reaction) is similar to the value obtained adding TBA. Adding phenol, the removal of CFA is significantly inhibited. The significant difference in abatement efficiency between MeOH/TBA and phenol indicates that surface-bound reactive radicals are dominant oxidation species, and that the electro/2,5Fe-2,5Cu/SBA/S₂O₈²⁻ oxidation reaction occurs near the catalyst surface.

EPR technique was used to confirm reactive radicals involved in the oxidation of CFA (Fig. 8). The presence of hydroxyl and sulfate radicals can be determined by the typical DMPO-SO₄ and DMPO-OH signals, based on their hyperfine splitting constants (DMPO-OH: aH = aN = 14.9 G; DMPO-SO₄: aN = 13.2 G, aH = 9.6 G, aH = 1.48 G, and aH = 0.78 G) [48,51]. After 5 min of reaction, EPR spectrum evidenced DMPO-OH signals (four lines, 1:2:2:1), indicating that hydroxyl radicals were generated after the beginning of the reaction. Since the intensity of the DMPO-OH signal is proportional to the hydroxyl radical concentration, Fig. 8 shows that the concentration of hydroxyl radicals decreases with the reaction time. Minor amount of sulfate radicals was detected at 5 min, but the DMPO-SO₄ signals disappeared at 10 min. Sulfate radicals can transform into hydroxyl radicals, at neutral pH, according to Eqs. (6) and (7). Also, DMPO-SO₄ adducts themselves can undergo rapid nucleophilic substitution (by H₂O/OH⁻) to form the hydroxyl radical adduct [52]. And finally, the absence of DMPO-SO₄ signal in EPR spectrum can originate from the too fast consumption of sulfate radicals by the pollutants, before scavenging [53].



3.5.2. Surface catalytic mechanism

The important role of surface-bound reactive radicals during the oxidation process of CFA is evidenced using quenching experiments. XPS analysis was performed to evaluate the impact of the reaction on the surface oxidation number of Fe and Cu species. Cu 2p and Fe 2p spectra, recorded over 2,5Fe-2,5Cu/SBA before and after reaction are presented in Fig. 9. Photpeak positions are corrected using the C 1s

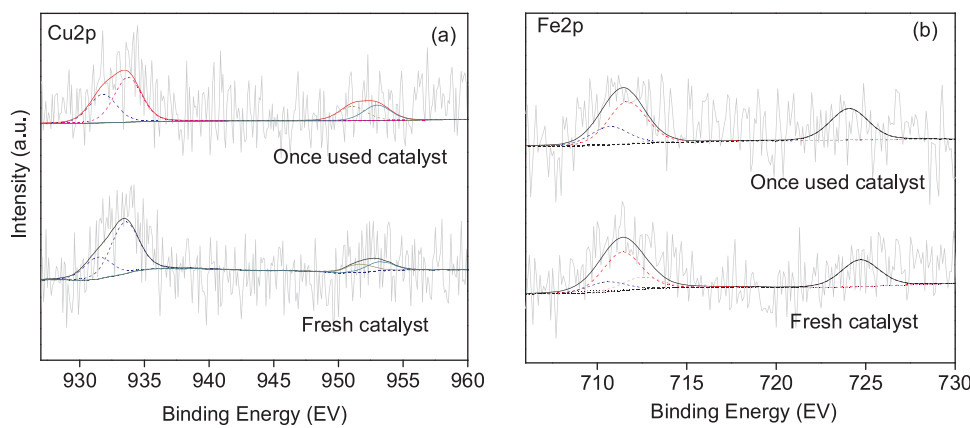


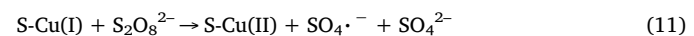
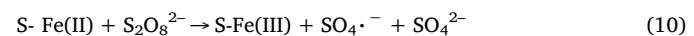
Fig. 9. Cu 2p (a) and Fe 2p (b) XPS spectra of 2,5Fe-2,5Cu/SBA catalyst, before and after 60 min of reaction.

signal arbitrary positioned at 284.6 eV [54].

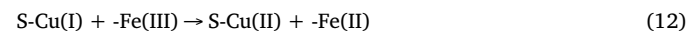
On fresh catalyst: the Cu 2p spectrum is resolved into two pair signals, with BE at 931.2 eV/951.3 eV, and 933.2 eV/953.1 eV. The former pair signals are assigned to Cu(I) species, and the latter are assigned to Cu(II) species [49,55,56]. Cu(I) proportion is evaluated at 37.7% of the total Cu species in the Cu 2p_{3/2} spectrum. Meanwhile, the Fe 2p_{3/2} photopeak is located at around 711.0 eV. Decomposition of the signal is performed using four contributions at BE located at: 709.6 eV, 710.2 eV, 711.3 eV and 712.1 eV [57–59]. Contributions at 709.6 eV and 710.3 eV are assigned to Fe(II) in ferrous oxide, while the main contribution, located around 711.0 eV, is assigned to Fe(III) in Fe₂O₃. Fe(II) species contribute to 20.3% of the total Fe species.

On used catalyst: modification of signals is observed. Most important modification concerns the evolution of the Fe(III)/Fe(II) and Cu(II)/Cu(I) ratios. After reaction, Fe(II) and Cu(I) proportion are observed to increase significantly, reaching values of 60.9% and 69.0%, respectively. Then, XPS analysis evidenced the reduction of ionic species on the catalyst surface during reaction. It is explained by the conversion of high- to low-charge metal species during the electrochemical process, as depicted in Fig. 10. Indeed, the mechanism of heterogeneous electro/2,5Fe-2,5Cu/SBA/S₂O₈²⁻ degradation of CFA is expected to proceed through the production of active radicals over metal ions. Similar with the Fenton-like process and the Haber-Weiss like mechanism [60–62], in neutral and basic solution, Fe(III) and Cu(II) will hardly activate the

PDS decomposition to sulfate radicals. The generation of sulfate radicals is then dependent on the capacity of Fe(III) or Cu(II) to be reduced by direct electron transfer in the solution (Eqs. (8) and (9)). In the heterogeneous catalyzed system, it is reasonable to presume that the redox cycles for iron and copper species will occur around the cathode side area. The interactions between PDS and Fe(II) or Cu(I) species will lead to the production of active radicals (Eqs. (10) and (11)):



Moreover, due to the presence of both metal ions in the catalyst, Fe(III) reduction by Cu(I) can also occur [63]:



It is worthy to note that the reaction of sulfate radical consumption for hydroxyl radical production (Eqs. (6) and (7)) is much more consequent under basic conditions. The generated free radicals (SO₄^{·-} and ·OH) were both present that explain the high efficiency at neutral to basic conditions.

3.6. The proposed degradation pathway of CFA

Considering our previous experience on the degradation of the CFA [6], the TOC removal efficiency of CFA remain relatively moderate, and several organic decomposition compounds were formed in solution. The identification of oxidation by-products/intermediates was performed by LC-MS analysis and the main products (Products 1–10), detected at both positive and negative ionization mode, were summarized in Table S1. Based on identified intermediates, CFA degradation during electro/2,5Fe-2,5Cu/SBA/S₂O₈²⁻ process could proceed by three different pathways (Fig. 11), which include C4-Cl bond breaking, aromatic ring cleavage and C1-O bond breaking. Fig. 11 indicates molecules or intermediates that were identified in this study (products 1–10 of Table S1) as well as over possible compounds formed during reaction and already identified in the literature (compound A to D of Fig. 11, [64–66]).

In Route I, dechlorination leads to the formation of 4-hydroxyphenoxyl-isobutyric acid (Product 2), which is further degraded into Product 3 and then Product A (not detected) with the oxidizing cleavage of aromatic ring. After undergoing a series of decarboxylation and carboxylation, maleic acid (Product 4) and 2-hydroxyisobutyric acid (Product 5) are formed.

In Route II, the addition of -OH group on the aromatic ring results in the generation of 2-(4-chloro-2-hydroxyphenoxy)-2-methylpropionic

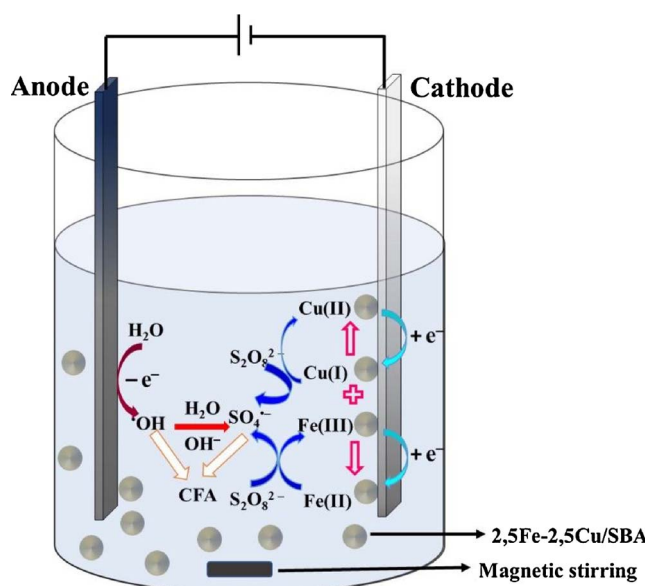


Fig. 10. Schematic representation of the electro/2,5Fe-2,5Cu/SBA/S₂O₈²⁻ process occurring for CFA degradation.

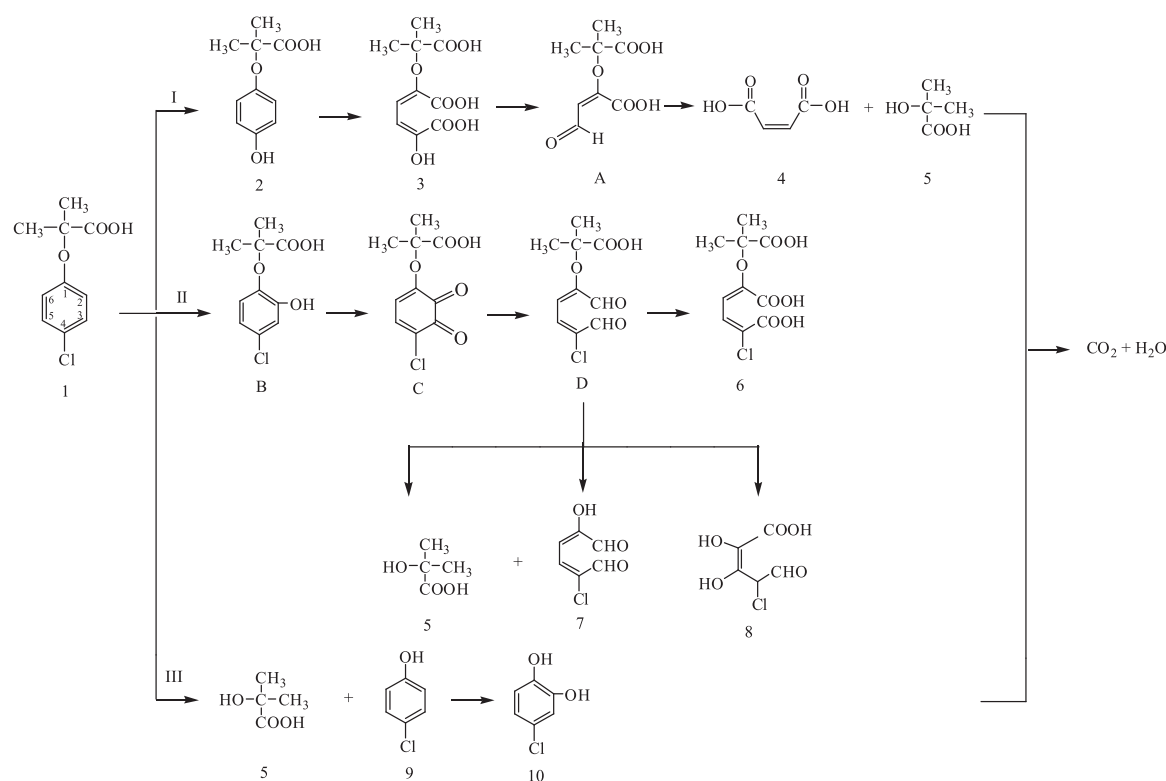


Fig. 11. Proposed degradation pathway of CFA in neutral aqueous medium, during the EC/2,5Fe-2,5Cu/SBA/S₂O₈²⁻ process.

acid (Product B, not detected). Subsequently, the adjacent carbon (C2 and C3) undergoes oxidation leading to the formation of Product C (not detected), and then the cleavage of aromatic ring produces the Product D (not detected). The further degradation of Product D gives rise to the formation of (i) Product 6 with the carbonyl groups being oxidized into carboxyl groups, and (ii) the generation of 2-hydroxyisobutyric acid (Product 5) with the breaking of C1-O bond, and Products 7 and 8 as well.

In Route III, the cleavage of C1-O bond gives rise to the formation of 4-chlorophenol (Product 9) and 2-hydroxyisobutyric acid (Product 5). Further attack on C2 position of 4-chlorophenol (Product 9) by hydroxyl radical leads to the generation of 4-chlorocatechol (Product 10). Finally, all the formed intermediates will be degraded to yield smaller carboxylic acids, CO₂ and H₂O.

4. Conclusions

Electro-assisted heterogeneous persulfate (electro/Fe-Cu catalyst/S₂O₈²⁻) process was studied for the degradation of clofibric acid, an emerging pollutant. Under these process conditions, CFA can be effectively degraded over a wide pH range, while removal efficiency increased with the PDS and catalyst concentrations. Compared with the monometallic Cu and Fe catalysts, the bimetallic Cu-Fe catalyst showed a higher catalytic activity, and the activity stability maintained over successive reaction cycles. Under optimized conditions of reaction, the removal efficiency achieved nearly 100% in a 60 min reaction. Results showed that CFA oxidation during the electro/catalyst/S₂O₈²⁻ process proceeds with C4-Cl bond breaking, aromatic ring cleavage and C1-O bond breaking steps. EPR analysis and quenching experiments allowed to detect hydroxyl radicals as main reactive radicals, with an activation of the oxidant at the catalyst surface. These observations also indicate the rapid conversion of surface radicals into hydroxyl radicals or its fast consumption. From the degrees of CFA removal reached under the electro/catalyst/S₂O₈²⁻ conditions, especially using the bimetallic Fe-Cu catalyst, this process may be regarded as an efficient process for the

oxidative degradation of organic contaminants in wastewater.

Acknowledgements

This work was supported by Natural Science Foundation of Hubei Province, China (Grant No. 2016CFB112), Postdoctoral Science Foundation of China (Grant No. 2016M602365) and Natural Science Foundation of China (Grant No. 21547006). The XPS analyses were partially supported by Large-scale Instrument and Equipment Sharing Foundation of Wuhan University. The authors also thank the National Center for Magnetic Resonance in Wuhan for EPR analysis. S. Royer and C. Ciotone acknowledge Chevreul Institute (FR 2638), Ministère de l'Enseignement Supérieur et de la Recherche, Région Nord – Pas de Calais and FEDER for funding.

Appendix A. Supplementary data

Supplementary material related to this article can be found, in the online version, at doi:<https://doi.org/10.1016/j.apcatb.2018.02.014>.

References

- [1] I. Sirés, E. Brillas, Environ. Int. 40 (2012) 212–229.
- [2] X. Yang, R.C. Flowers, H.S. Weinberg, P.C. Singer, Water Res. 45 (2011) 5218–5228.
- [3] I. Sirés, F. Centellas, J.A. Garrido, R.M. Rodríguez, C. Arias, P.-L. Cabot, E. Brillas, Appl. Catal. B: Environ. 72 (2007) 373–381.
- [4] R. Rosal, M.S. Gonzalo, K. Boltes, P. Letón, J.J. Vaquero, E. García-Calvo, J. Hazard. Mater. 172 (2009) 1061–1068.
- [5] R. Salgado, A. Oehmen, G. Carvalho, J.P. Noronha, M.A.M. Reis, J. Hazard. Mater. 241–242 (2012) 182–189.
- [6] H. Lin, J. Wu, H. Zhang, Chem. Eng. J. 244 (2014) 514–521.
- [7] G.P. Anipsitakis, D.D. Dionysiou, Environ. Sci. Technol. 38 (2004) 3705–3712.
- [8] L.W. Matzek, K.E. Carter, Chemosphere 151 (2016) 178–188.
- [9] L. Ismail, C. Ferronato, L. Fine, F. Jaber, J.-M. Chovelon, Appl. Catal. B: Environ. 201 (2017) 573–581.
- [10] I.M. Kolthoff, I.K. Miller, J. Am. Chem. Soc. 73 (1951) 3055–3059.
- [11] L.W. Hou, H. Zhang, X.F. Xue, Sep. Purif. Technol. 84 (2012) 147–152.
- [12] A. Tsitonaki, B. Petri, M. Crimi, H. Mosbæk, R.L. Siegrist, P.L. Bjerg, Crit. Rev.

Environ. Sci. Technol. 40 (2010) 55–91.

[13] B.-T. Zhang, Y. Zhang, Y. Teng, M. Fan, Crit. Rev. Environ. Sci. Technol. 45 (2015) 1756–1800.

[14] J.C. Yan, M. Lei, L.H. Zhu, M.N. Anjum, J. Zou, H.Q. Tang, J. Hazard. Mater. 186 (2011) 1398–1404.

[15] H. Zhang, C.Z. Fei, D.B. Zhang, F. Tang, J. Hazard. Mater. 145 (2007) 227–232.

[16] E. Brillas, I. Sirés, M.A. Oturan, Chem. Rev. 109 (2009) 6570–6631.

[17] S. Chou, Y.-H. Huang, S.-N. Lee, G.-H. Huang, C. Huang, Water Res. 33 (1999) 751–759.

[18] Y.-J. Shih, C.-P. Lin, Y.-H. Huang, Sep. Purif. Technol. 104 (2013) 100–105.

[19] C. Trellu, Y. Péchaud, N. Oturan, E. Mousset, D. Huguenot, E.D. van Hullebusch, G. Esposito, M.A. Oturan, Appl. Catal. B: Environ. 194 (2016) 32–41.

[20] H. Zhang, Z. Wang, C.C. Liu, Y.Z. Guo, N. Shan, C.X. Meng, L.Y. Sun, Chem. Eng. J. 250 (2014) 76–82.

[21] J. Wu, H. Zhang, J.J. Qiu, J. Hazard. Mater. 215–216 (2012) 138–145.

[22] H. Lin, J. Wu, H. Zhang, Sep. Purif. Technol. 117 (2013) 18–23.

[23] W.-D. Oh, Z. Dong, T.-T. Lim, Appl. Catal. B: Environ. 194 (2016) 169–201.

[24] J. Wang, C. Liu, L. Tong, J.S. Li, R. Luo, J.W. Qi, Y. Li, L.J. Wang, RSC Adv. 5 (2015) 69593–69605.

[25] J. Wang, C. Liu, J.S. Li, R. Luo, X.R. Hu, X.Y. Sun, J.Y. Shen, W.Q. Han, L.J. Wang, Appl. Catal. B: Environ. 207 (2017) 316–325.

[26] E.G. Garrido-Ramírez, J.F. Marco, N. Escalona, M.S. Ureta-Zañartu, Micro. Meso. Mater. 225 (2016) 303–311.

[27] Y. Wang, H. Zhao, G. Zhao, Appl. Catal. B: Environ. 164 (2015) 396–406.

[28] S. Karthikeyan, M.P. Pachamuthu, M.A. Isaacs, S. Kumar, A.F. Lee, G. Sekaran, Appl. Catal. B: Environ. 199 (2016) 323–330.

[29] J. Wang, C. Liu, I. Hussain, C. Li, J. Li, X. Sun, J. Shen, W. Han, L. Wang, RSC Adv. 6 (2016) 54623–54635.

[30] L.X. Hu, F. Yang, W.C. Lu, Y. Hao, H. Yuan, Appl. Catal. B: Environ. 134–135 (2013) 7–18.

[31] Y. Feng, D.L. Wu, Y. Deng, T. Zhang, K. Shih, Environ. Sci. Technol. 50 (2016) 3119–3127.

[32] H. Lin, H. Zhang, L.W. Hou, J. Hazard. Mater. 276 (2014) 182–191.

[33] C. Ciotoanea, B. Dragoi, A. Ungureanu, A. Chiriac, S. Petit, S. Royer, E. Dumitriu, Chem. Commun. 49 (2013) 7665–7667.

[34] L. Xiang, S. Royer, H. Zhang, J.M. Tatibouët, J. Barrault, S. Valange, J. Hazard. Mater. 172 (2009) 1175–1184.

[35] M. Bonne, D. Sellam, J.-P. Dacquin, A.F. Lee, K. Wilson, L. Olivi, A. Cognigni, P. Marécot, S. Royer, D. Duprez, Chem. Commun. 47 (2011) 1509–1511.

[36] L.W. Hou, H. Zhang, L.G. Wang, L. Chen, Y. Xiong, X.F. Xue, Sep. Purif. Technol. 117 (2013) 46–52.

[37] N. Wahba, M.F. El Asmar, M.M. El Sadr, Anal. Chem. 31 (1959) 1870–1871.

[38] X. Zhong, J. Barbier Jr., D. Duprez, H. Zhang, S. Royer, Appl. Catal. B: Environ. 121–122 (2012) 123–134.

[39] R.M. Malek Abbaslou, A. Tavasoli, A.K. Dalai, Appl. Catal. A: Gen. 355 (2009) 33–41.

[40] H.H.P. Yiu, M.A. Keane, Z.A.D. Lethbridge, M.R. Lees, A.J.E. Haj, J. Dobson, Nanotechnology 19 (2008) 255606.

[41] S.M. Ciocilteu, M. Salou, Y. Kiyozumi, S.-I. Niwa, F. Mizukami, M. Haneda, J. Mater. Chem. 13 (2003) 602–607.

[42] S. Kiaphuengporn, M. Charoenpanich, J. Limtrakul, Chem. Eng. J. 240 (2014) 527–533.

[43] J.-S. Kim, S. Lee, S.-B. Lee, M.-J. Choi, K.-W. Lee, Cata. Today 115 (2006) 228–234.

[44] M.M. Villaverde, N.M. Bertero, T.F. Garetto, A.J. Marchi, Catal. Today 213 (2013) 87–92.

[45] J. Wu, H. Zhang, N. Oturan, Y. Wang, L. Chen, M.A. Oturan, Chemosphere 87 (2012) 614–620.

[46] L. Zhou, M. Sleiman, C. Ferronato, J.-M. Chovelon, P. de Sainte-Claire, C. Richard, Water Res. 123 (2017) 715–723.

[47] S.Y. Yang, T. Xiao, J. Zhang, Y.Y. Chen, L. Li, Sep. Purif. Technol. 143 (2015) 19–26.

[48] Y. Xu, J. Ai, H. Zhang, J. Hazard. Mater. 309 (2016) 87–96.

[49] N.N. Binitha, S. Sugunan, Microporous Mesoporous Mater. 93 (2006) 82–89.

[50] C. Liang, H.-W. Su, Ind. Eng. Chem. Res. 48 (2009) 5558–5562.

[51] Y.X. Wang, H.Q. Sun, X.G. Duan, H.M. Ang, M.O. Tadé, S.B. Wang, Appl. Catal. B: Environ. 172 (2015) 73–81.

[52] G.S. Timmins, K.J. Liu, E.J.H. Bechara, Y. Kotake, H.M. Swartz, Free Radic. Biol. Med. 27 (1999) 329–333.

[53] Y.X. Wang, L. Zhou, X.G. Duan, H.Q. Sun, E.L. Tin, W.Q. Jin, S.B. Wang, Catal. Today 258 (2015) 576–584.

[54] J. Fernandez, J. Bandara, A. Lopez, P. Buffat, J. Kiwi, Langmuir 15 (1998) 185–192.

[55] M. Xia, M.C. Long, Y.D. Yang, C. Chen, W.M. Cai, B.X. Zhou, Appl. Catal. B: Environ. 110 (2011) 118–125.

[56] Q. Ye, L.N. Yan, F.F. Huo, H.P. Wang, S.Y. Cheng, T.F. Kang, Acta Chim. Sinica 69 (2011) 1524–1532.

[57] L.Q. Guo, F. Chen, X.Q. Fan, W.D. Cai, J.L. Zhang, Appl. Catal. B: Environ. 96 (2010) 162–168.

[58] H.Y. Zhao, Y.J. Wang, Y.B. Wang, T.C. Cao, G.H. Zhao, Appl. Catal. B: Environ. 125 (2012) 120–127.

[59] J. Li, Q. Liu, Q.Q. Ji, B. Lai, Appl. Catal. B: Environ. 200 (2017) 633–646.

[60] S.-S. Lin, M.D. Gurrol, Environ. Sci. Technol. 32 (1998) 1417–1423.

[61] W.P. Kwan, B.M. Voelker, Environ. Sci. Technol. 37 (2003) 1150–1158.

[62] E. Isarain-Chávez, C. Arias, P.L. Cabot, F. Centellas, R.M. Rodríguez, J.A. Garrido, E. Brillas, Appl. Catal. B: Environ. 96 (2010) 361–369.

[63] Z.B. Han, Y.C. Dong, S.M. Dong, J. Hazard. Mater. 189 (2011) 241–248.

[64] M.S. Yalfani, S. Contreras, J. Llorca, F. Medina, Appl. Catal. B: Environ. 107 (2011) 9–17.

[65] Q.Q. Sun, Y. Wang, L.S. Li, J.S. Bing, Y.X. Wang, H.H. Yan, J. Hazard. Mater. 286 (2015) 276–284.

[66] S.S. Sable, P.P. Ghute, P. Álvarez, F.J. Beltrán, F. Medina, S. Contreras, Catal. Today 240 (2015) 46–54.